Integrated air-bridge tandem thermophotovoltaics with high efficiency over a broad heat source temperature range

Bosun Roy-Layinde[1,4], Jihun Lim[2,4], Andrej Lenert[2*], and Stephen R. Forrest[2,3*]

[1]Department of Chemical Engineering, University of Michigan, Ann Arbor, MI 48109

[2]Department of Electrical Engineering and Computer Science, University of Michigan, Ann Arbor, MI 48109

[3]Department of Physics and Materials Science and Engineering, University of Michigan, Ann Arbor, MI 48109

[4]These authors contributed equally: Bosun Roy-Layinde, Jihun Lim.

[*]Corresponding authors: Stephen R. Forrest (stevefor@umich.edu), Andrej Lenert (alenert@umich.edu)

AUTHOR INFORMATION

Corresponding Authors

Stephen R. Forrest – *Department of Electrical Engineering and Computer Science, University of Michigan, Ann Arbor, Michigan 48109, United States; Department of Physics, University of Michigan, Ann Arbor, Michigan 48109, United States*; orcid.org/0000-0003-0131-1903; Email: stevefor@umich.edu

Andrej Lenert – *Department of Chemical Engineering, University of Michigan, Ann Arbor, Michigan 48109, United States*; orcid.org/0000-0002-1142-6627; Email: alenert@umich.edu

Authors

Bosun Roy-Layinde – *Department of Chemical Engineering, University of Michigan, Ann Arbor, Michigan 48109, United States*; orcid.org/0000-0003-2388-0218

Jihun Lim – *Department of Electrical Engineering and Computer Science, University of Michigan, Ann Arbor, Michigan 48109, United States*; orcid.org/0000-0003-4074-9617

Abstract

Mechanically stacked, tandem thermophotovoltaic (TPV) cells featuring integrated air-bridge InGaAs and InGaAsP subcells achieve high spectral efficiency and emission temperature versatility. Thermocompression bonding of electrodes on opposing single cells integrates air layers, boosting out-of-band reflectance (R_{OUT}) compared to cells lacking air bridges. We report a 0.74/0.74 eV homotandem exhibiting R_{OUT} = 96.4%. When operated in a multiterminal arrangement, the homotandem achieves 38% efficiency, marking a 20% absolute improvement over a comparable two-terminal configuration. We also demonstrate a 0.9/0.74 eV heterotandem with R_{OUT} = 97.2% and spectral efficiencies approaching 80%. By minimizing losses associated with parasitic absorption and current mismatch, it substantially expands the emission temperature range while preserving high efficiency. This leads to a reduction in the cost of the energy storage medium in thermal batteries by over 40%. The air-bridge tandem technology paves the way for high-performing tandem cells compatible with a variety of heat sources unrestricted by the choice of subcell materials.

Thermophotovoltaic cells (TPVs) are a solid-state approach to converting heat to electricity. They have the potential to offer high-performance, modular, and near-instantaneous power-delivery using a range of heat sources, including stored thermal energy[1]. These features are advantageous for regulating the supply of intermittent renewables such as wind and solar[2]. Recently demonstrated thin-film TPV cells supported by highly reflective substrates have produced broadband improvements in spectral utilization and correspondingly large gains in TPV efficiency[3–12]. The key to realizing these improvements is high reflectivity of out-of-band radiation (R_{OUT}) corresponding to the fraction of incident radiation at energies below the TPV bandgap that is not absorbed by the semiconductor, and thus is returned to the heat source with low loss. This approach is termed photon recovery (or recuperation) because the radiation is returned to the heat source until it is reemitted at a sufficiently high energy to excite electrons across the bandgap (called in-band radiation).

Realizing efficient photon recovery in multijunction cells has the potential to further broaden the application space for TPVs and maximize their potential in renewable energy applications such as in grid-scale energy storage (thermal batteries). Recently, 1.4/1.2 eV and 1.2/1.0 eV bandgap multijunction cells reported by LaPotin *et al* demonstrated 41% and 39% TPV efficiency under 2000°C illumination[12]. As in conventional multijunction solar cells, these TPV cells used a highly doped semiconductor tunnel junction for series connection between the top and bottom subcells comprising the tandem. Unfortunately, tunnel junctions introduce substantial parasitic free carrier absorption below the bandgap, which significantly degrades R_{OUT} and limits their efficiency[13–15]. Furthermore, the current matching constraint imposed by traditional series-connected subcells limits the range of emitter temperatures over which high efficiency is maintained (which we refer to as the "emission-temperature range").

Increasing the emission temperature range is particularly important in thermal batteries relying on TPV converters and sensible heating/cooling of an insulated storage medium (e.g., graphite). Such thermal batteries capture excess electrical energy from the grid through resistive heating of the storage medium. The stored energy is subsequently returned to the grid by employing TPVs to convert the thermal radiation emitted from the storage media back into electricity. In such uses, a larger emission temperature range produces higher specific battery capacities and concomitantly lower energy storage costs.

To enable high performance over a wide emission-temperature range, we demonstrate mechanically bonded tandem air-bridge TPV cells that eliminate the tunnel junction, and allow for separate contacts to each subcell, thus eliminating the current matching constraint[16]. The tunnel junctions used in conventional, monolithic group III-V multijunction cells are replaced by a patterned metal electrode grid to connect the subcells as shown in Figure 1(a). Thus, the cells are individually separated by air-bridges, which significantly increase the R_{OUT} compared to conventional cells with a single metallic back surface reflector. Additionally, the three metal layers facilitate interconnecting the cell in either two-terminal (2T) or multiterminal (3T and 4T) configurations by inserting connections at the layer junctions. The detailed process steps are described in Supporting Information 1.

Overall, the dual air-bridge architecture offers several advantages over analogous TPV cells. The first is that it reflects nearly all the radiation that is not absorbed within the subcell active layers. We show that eliminating the tunnel junction avoids a >3% loss in R_{OUT}. Due to reduced thermalization losses and comparably high R_{OUT}, the resulting tandem cells show enhanced spectral efficiencies exceeding those of its single-junction air-bridge counterparts[3,4,10,16]. Another is that a multiterminal configuration eliminates current-matching constraints that limit performance when the emission temperature varies, as in the cooling/discharge phase of thermal batteries[18,19]. Together, these advantages combine to allow the emission temperature to range over 600°C while maintaining an average efficiency within 3% of its peak. Finally, thermocompression (cold-weld) bonding of subcells allows for their integration based on entirely different materials systems (e.g., III-Vs and Si) for each subcell[17], which provides flexibility when optimizing tandems for both cost and performance.

To better understand the potential of replacing tunnel junctions with nanoscale air gaps, optical simulations of various TPV structures are used to evaluate parasitic absorption in conventional and air-bridge devices. In the tandem configuration, the bottom cell consists of a 2-µm- thick 0.74 eV energy gap $In_{0.53}Ga_{0.47}As$ (hereafter referred to as InGaAs) absorption layer, whereas the top cell comprises an InGaAs absorber (forming a homotandem), or an 0.9 eV $In_{0.69}Ga_{0.31}As_{0.67}P_{0.33}$ (referred to as InGaAsP) absorber (forming a heterotandem cell). The simulations assume negligible free carrier absorption (FCA) in the lightly doped absorber layers, while FCA is estimated using a Drude model[18] [18]for the tunnel-junction (TJ) layer. The simulated R_{OUT} is therefore an upper bound for these structures.

The simulation results are shown in Figure 1(b). The heterotandem cell exhibits a slightly higher R_{OUT} than the single air-bridge cell with a 2-µm thick InGaAs absorber. The additional air-semiconductor interfaces in the heterotandem cell reduce the optical power reaching the Au back reflector/electrode, which diminishes parasitic absorption in that layer. Conversely, the homotandem cell shows a slightly lower R_{OUT} than the single air-bridge cell. This difference

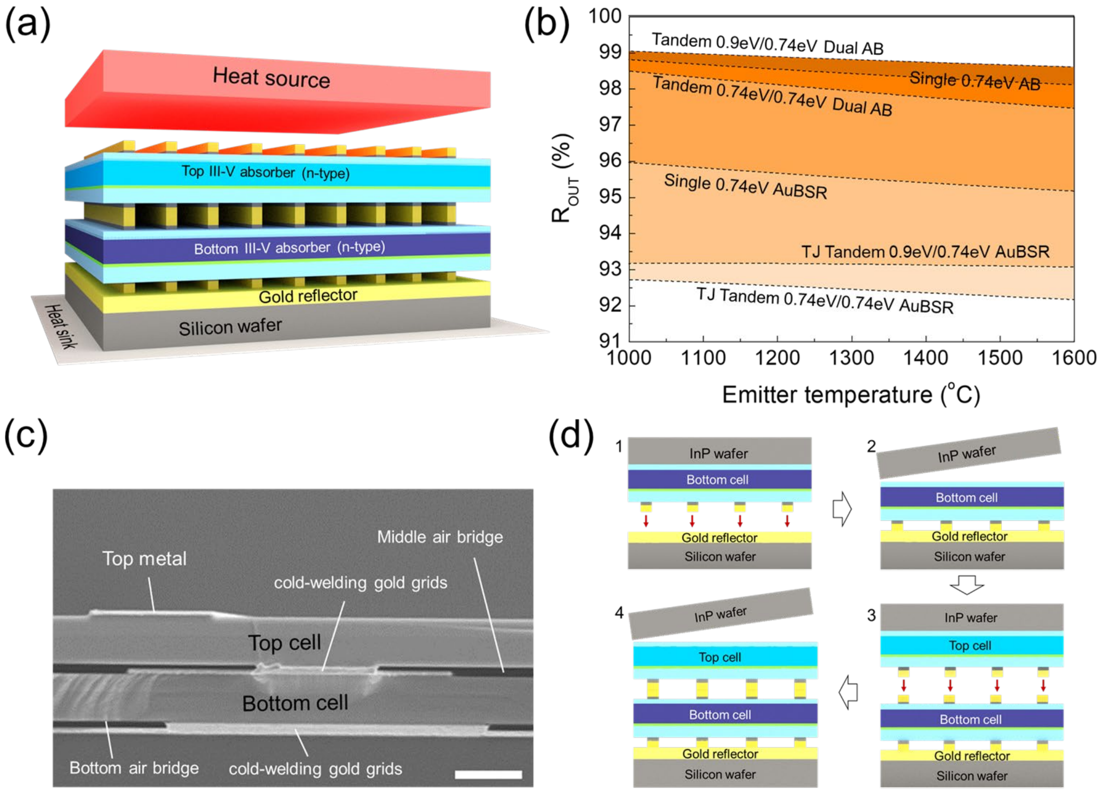

Fig. 1 Tandem air-bridge TPV structure and fabrication. (a) Schematic of the thermal system consisting of a heat source and an air-bridge tandem TPV cell attached to a heat sink. The top and bottom cells are cold-weld bonded at the middle grid. (b) Simulated out-of-band reflectance (R_{OUT}) as a function of emitter temperature for the air-bridge (AB) cells and those with a conventional gold back surface reflector (AuBSR). (c) Cross-sectional scanning electron microscope (SEM) image of an air-bridge tandem. Scale bar: 5 µm. (d) Illustration of the cold-welding and epitaxial layer liftoff process for fabricating the tandem cell. The epitaxial layer composition and detailed process steps are in Supporting Information 1.

can be largely attributed to increasing the total InGaAs thickness from 2 to 4 µm, which results in higher parasitic absorption near the InGaAs band edge. Despite the relatively low R_{out}, the homotandem cell offers the advantage of a higher power density than a single cell. While a two terminal homotandem cell necessitates current-matched subcells, this requirement is eliminated using four terminals[18,19]. In the tandem cell, distinct optical cavity modes are also formed by the top and bottom cells (see Supporting Information 2 for additional discussion). In contrast to the air-bridge cells, the R_{OUT} in the simulated TJ tandems is limited to < 94%, which is consistent with experimental observations[11,12,19,20]. To compare optical simulations against experiment, homo- and heterotandem air-bridge cells are demonstrated and characterized. Figure 1(c) shows a scanning electron microscope (SEM) cross-section image of the tandem cell where the semiconductor membranes are mechanically supported by Au gridlines with no discernible compressive deformation, fracturing or buckling[10]. All layers are grown by metalorganic chemical vapor deposition lattice-matched to (100) Fe-doped InP substrates. Figure 1(d) illustrates the fabrication sequence showing multiple cold welding and epitaxial layer liftoff steps, as described previously[3,4,10]. Given that the Si substrate is thermally conductive and mechanically stable, the buckling in the membranes is suppressed by adjusting the thickness of the III-V thin film and the cold-welding conditions[21]. The three layers of gridlines are optically aligned prior to bonding to optimize the geometrical fill factor (GFF), defined as the ratio of the gridline to the total device area. Note that misaligned gridlines at the junction between subcells will shadow the bottom cell, leading to an increase of series resistance and a reduction in cell quantum efficiency. Bonding at a temperature of 150°C and pressure of 3 MPa produces the middle metal grid consisting of Ti(10 nm)/Au(300 nm)/Au(300 nm)/Ti(10 nm). Importantly, the gold surfaces must be kept free of contamination and dust to minimize pressure used in the welding process. Finally, the cell mesa is patterned through wet-etching of InGaAsP and InGaAs.

Figure 2(a) shows the measured absorption spectrum and external quantum efficiency (EQE) of the InGaAs homotandem cell. The top and bottom cells absorb 61% and 10% of the incident in-band light, respectively. When weighted to a 1223°C blackbody illumination source, the out-of-band reflectance is 96.4%, which corresponds to a parasitic out-of-band absorption of A_{OUT} = 3.6%. Compared to our previous report[3], the tandem has an additional parasitic

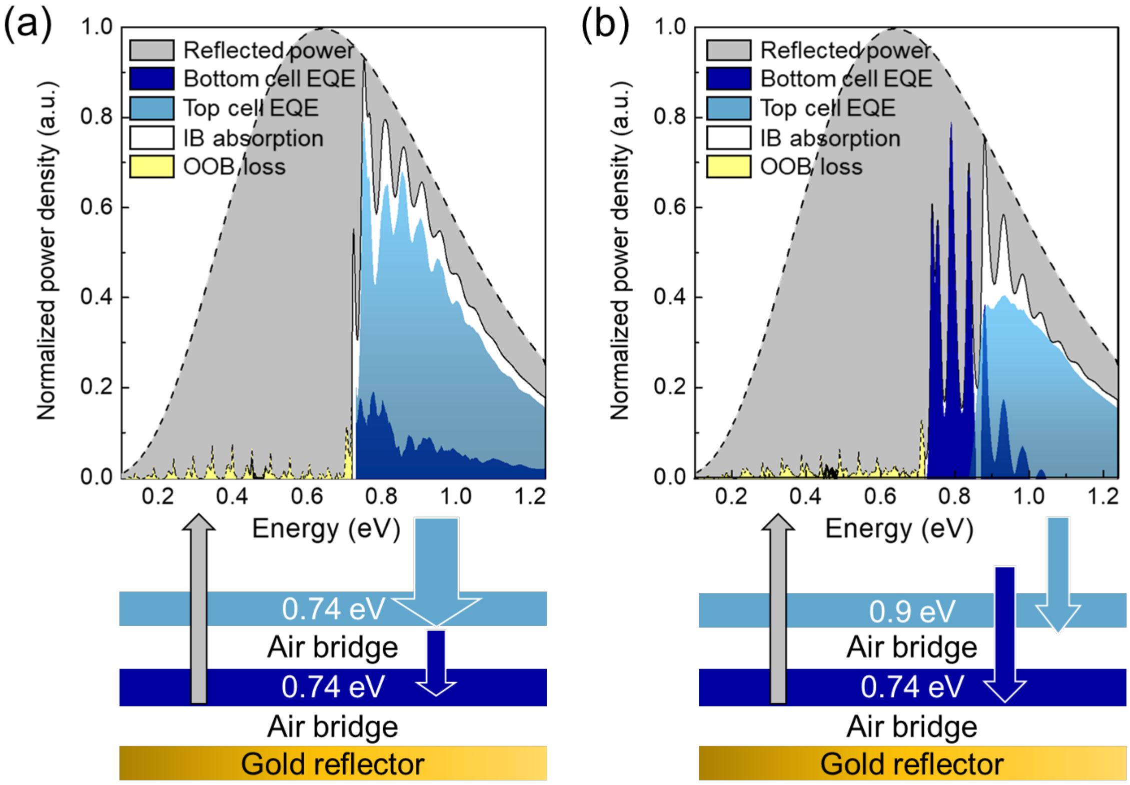

Fig. 2 Photon utilization in the homo- and heterotandem cells. (a) and (b) Spectral power breakdown in the homo- and heterotandem cell, respectively. The dashed line denotes the incident 1223°C blackbody spectrum. EQE measurements for individual subcells reveal spectral splitting in each tandem cell. In-band (IB) absorption and out-of-band (OOB) loss are characterized via FTIR spectroscopy at wavelengths of 1.0–15.5 μm. The optical cavities formed by the semiconductor membranes, the Au reflector, and two air gaps lead to the interference features.

absorption in the out-of-band region of $A_{\mathrm{out}} = 2\%$. Out-of-band losses (depicted by the yellow shaded region), exceeding those predicted by simulations, are mostly attributed to FCA stemming from residual background carriers[22]. Absorption by defects near the band edge contributes $A_{\mathrm{OUT}} < 0.3\%$, while FCA by free charges and impurities accounts for 1.4%. The calculated spectral efficiency (*SE*) for this tandem is 68.4% which is comparable to its single-junction counterpart (see Methods, and Supporting Information 2). For context, a representative monolithic tandem featuring a tunnel junction and gold back surface reflector (AuBSR) shows a calculated *SE* = 62.3% (see Supporting Information 2). The measured absorption and EQE of the heterotandem cell are presented in Figure 2(b). The use of two different bandgaps leads to more balanced absorption than in the homotandem. For example, under 1223°C illumination, the top and bottom subcells absorb 33% and 38% of the in-band spectrum, respectively. The cell achieves R_{OUT} = 97.2%, which is 0.8% higher than for the homotandem, consistent with the simulation in Figure 1(b). Absorption by defects near the band edge contributes A_{OUT} = 0.1%, while FCA accounts for 1.4%. The combination of high R_{OUT} and lower thermalization losses yields a simulated SE = 78% at 1223°C. Considering the increased parasitic absorption observed in the experiment, the SE decreases to 74% (see Supporting Information 2). Nonetheless, the addition of the 0.9 eV top cell enhances the SE by >4% relative to both the 0.74 eV single-junction and homotandem air-bridge cells. Overall, these results highlight the photon-utilization advantages offered by the dual air-bridge tandem design.

Figure 3(a) shows the current density versus voltage (J-V) characteristics of the 2T homotandem cell and its constituent subcells. Device performance parameters, including saturated dark currents and series resistance (R_s), are used as input parameters in simulations shown by the dashed lines (see Supporting Information 3). Due to the partial transparency of the top cell, the homotandem exhibits a notable imbalance in short-circuit current density (J_{sc}) between its subcells across all emitter temperatures (Fig. 3b). Consequently, the top subcell achieves a slightly higher open circuit voltage (V_{oc}) than the bottom cell (Fig. 3c). We note, however, that the subcells produce almost identical V_{oc} at the same photocurrent (see Supporting Information 3), indicating their similar material qualities. The measured V_{oc} in the 2T configuration exceeds 1 V and is equivalent to the sum of V_{oc} from each subcell, as expected for series tandem configurations with very low loss. The higher output voltage is a key advantage of the homotandem device compared to its single-junction counterpart because of its potential to substantially decrease series resistance (see Supporting Information 3).

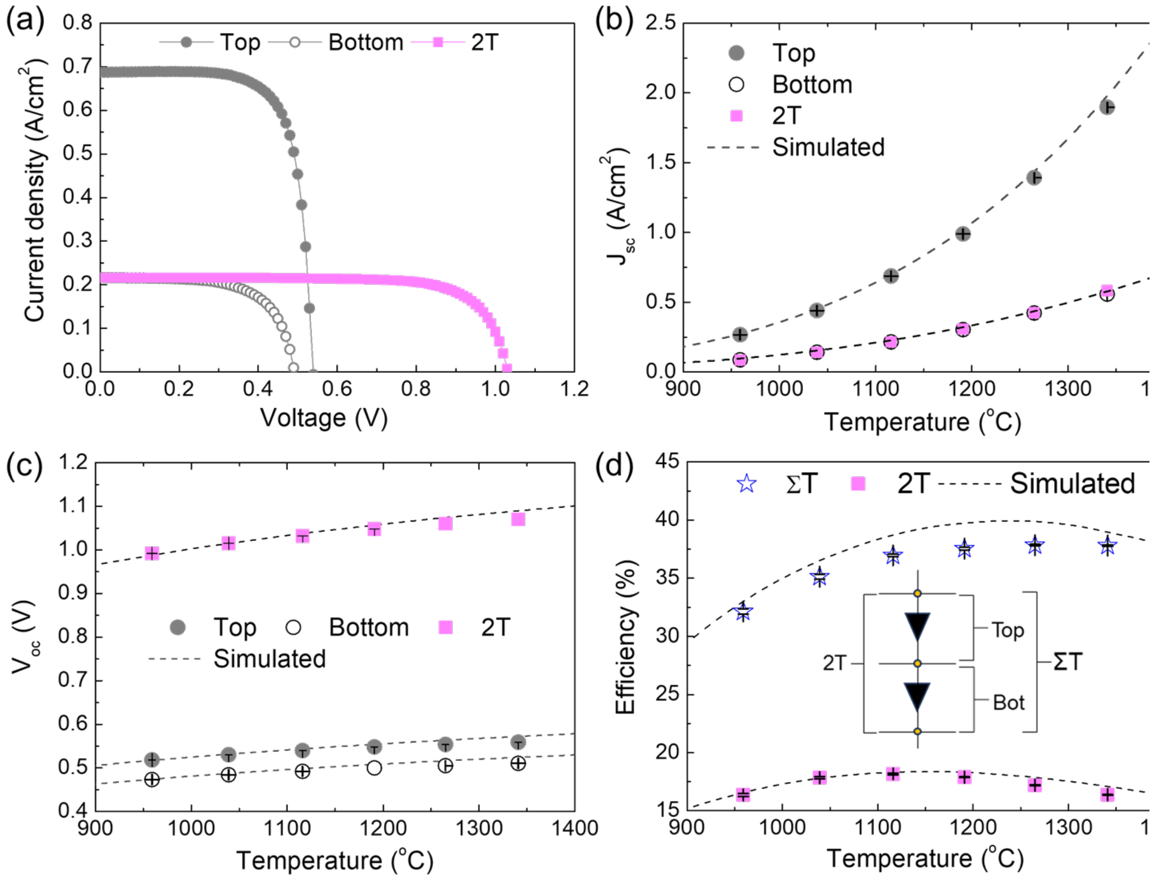

Fig. 3 Homotandem device performance characterization. (a) Current-voltage measurements under 1120°C illumination. (b) Short-circuit current density (J_{sc}) and (c) open-circuit voltage (V_{oc}) of the tandem and the individual subcells as a function of emitter temperature. (d) Power conversion efficiency vs. emitter temperature in both 2T and multi-terminal (ΣT) configurations. Simulated characteristics are shown by dashed lines. Complete experimental results for these cells are provided in Supporting Information 3.

The TPV efficiency of the homotandem is shown in Figure 3(d). Here, the efficiency is defined by the ratio of maximum output electrical power to the heat absorbed by the cell, in which the latter is determined from optical measurements (see Methods). The inset indicates two operation modes of the dual air-bridge cells: series-connected 2T and in the multiterminal configuration (ΣT). Here, ΣT indicates the sum of the individual maximum power points (P_{MPP})

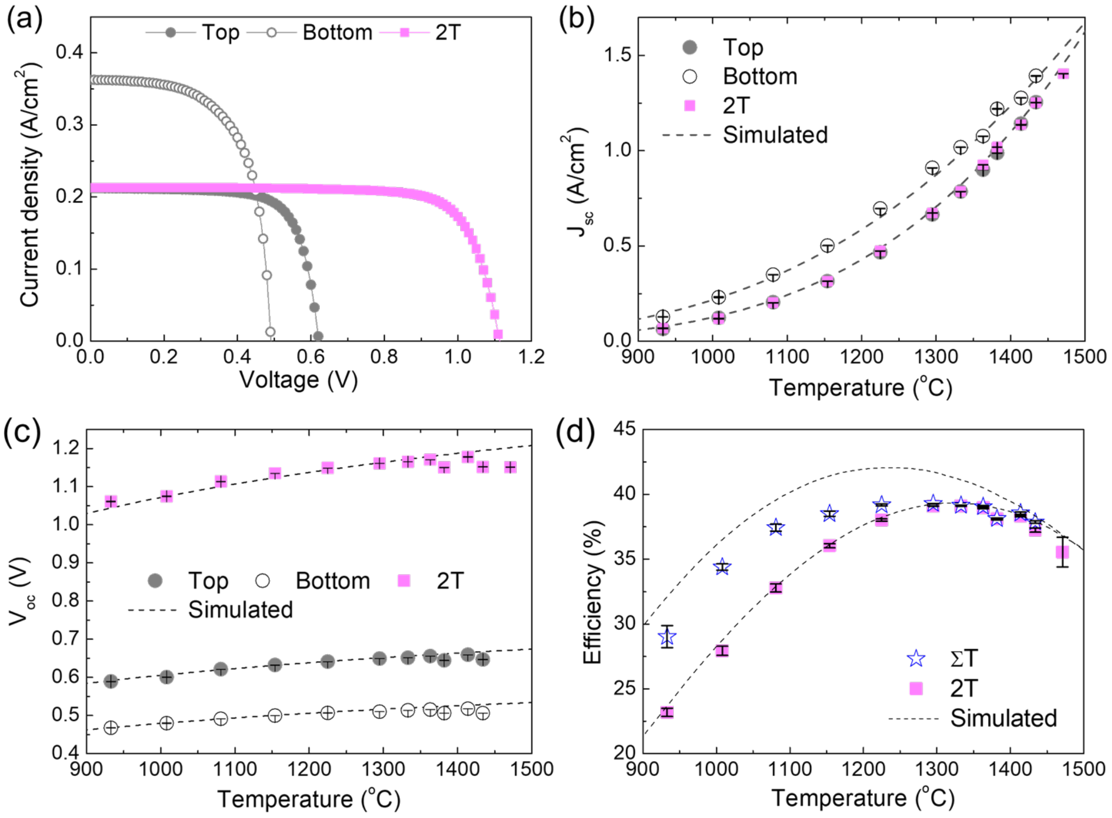

Fig. 4 Heterotandem device performance characterization. (a) Current-voltage measurements under 1155°C irradiation. (b) J_{sc} and (c) V_{oc} of the tandem and subcells vs. emitter temperature. (d) Power conversion efficiency vs. emitter temperature for both 2T and multi-terminal configurations. Simulated characteristics are shown by dashed lines.

of the top and bottom cells, representing an upper bound achievable in this configuration, where the resistance losses by wires and contacts are ignored[23–25]. The current imbalance in 2T operation limits the output power and efficiency under 1120°C illumination to 0.2 W/cm^2 and 18.2 ± 0.1%, respectively. In contrast, the ΣT configuration enables each cell to operate at its respective P_{MPP}, yielding a power density of 0.7 W/cm^2 and a peak efficiency of 37.8 ± 0.2% at 1265°C. This represents a 2% absolute improvement over a 0.74 eV single-junction air-bridge cell at the same emitter temperatures (see Supporting Information 3). The homotandem efficiency drops at higher temperatures and view factors due to an unoptimized R_s (45 mΩ-cm^2 and 130 mΩ-cm^2 for top and bottom cells, respectively), leading to a decrease in fill factor *FF*. The relatively high R_s for the bottom cell is attributed to the absence of Pt in the metal grids between the subcells[26], which was avoided due to inconsistencies with the Pt deposition process. The R_s can be reduced by optimizing the metal contact structure (such as adding Pt or Pd)[26], by post-contact annealing[27] and reducing the grid pitch[18,28]. Among these methods, optimizing the metal contact structure and reducing the grid pitch do not compromise the mechanical stability of thin-film membranes that span the gridlines[21]. Our simulations indicate that reducing the series resistance to comparable levels as the single junction cell and optimizing the thickness of the top absorber layer can yield efficiencies of 43% for the ΣT InGaAs homotandem (see Supporting Information 4). Effective thermal management also reduces the effects of series resistance and non-radiative recombination losses. This result highlights the potential for further optimization of the InGaAs homotandem and its application to other single-junction cells with more optimized bandgaps, to enhance their peak efficiency. The heterotandem *J-V* results are shown in Figures 4(a). The current mismatch is smaller than in the homotandem device (Fig. 4b), particularly at higher emitter temperatures. The V_{oc} of the 0.9 eV energy gap top cell is approximately 100 mV larger than for the 0.74 eV bottom cell across the range of temperatures shown in Fig. 4c. At higher temperatures, the individual subcells exhibit comparable bandgap-offset voltages (*i.e.*, the difference between the bandgap and V_{oc}), approaching 220 mV. The V_{oc} in the 2T configuration exceeds 1.1 V and is equivalent to the sum of the V_{oc} in the top and bottom subcells. The efficiencies of the 2T and ΣT heterotandems are shown in Fig. 4d. The configurations show similar efficiency under 1300-1400°C illumination, where the incident spectrum is more evenly split between the absorption bands of the subcells (see Fig. 4b). Thus, both the 2T and multiterminal arrangements of the heterotandem achieve power densities of 0.7 W/cm^2 a peak efficiency of 39.1 ± 0.2% under 1330°C illumination (see Supporting Information 5). At lower temperatures, the ΣT tandem exhibits higher efficiency than the 2T configuration by mitigating the impact of current mismatch. Notably, the ΣT heterotandem maintains >36% efficiency and >0.3 W/cm^2 at emission temperatures as low as 1100°C. This improvement leads to an average efficiency of 37% over the range of 1000°C to 1600°C, which is 2% higher than that for 2T.

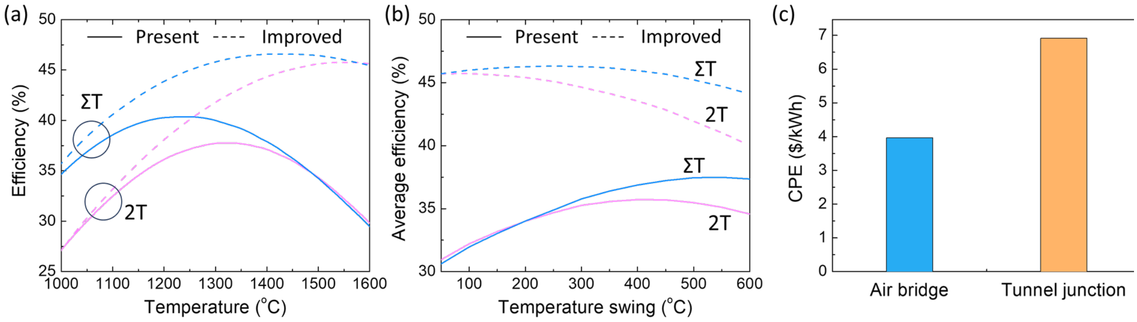

Fig. 5 Power conversion efficiency in a thermal battery and estimated cost per unit of energy. (a) Present day efficiency of the air-bridge heterotandem (solid lines) versus emitter temperature, and that expected with reduction in cell series resistance to 15 mΩ-cm^2 (dashed lines). (b) Average efficiency as a function of temperature swing during the cooling phase, assuming an initial storage temperature of 1600°C. The multi-terminal configuration has lower sensitivity to spectral variations during the wide temperature discharge of thermal batteries. (c) Estimated cost of graphite per unit energy (CPE), comparing the air-bridge heterotandem to an analogous tunnel-junction tandem device. This calculation assumes a 600°C temperature swing with a $0.5/kg cost of graphite.

Figure 5(a) illustrates that a reduction in series resistance (R_S = 15 mΩ-cm^2 for each subcell) can lead to efficiencies >45% for the ΣT heterotandem. This also shifts the optimum performance towards higher emitter temperatures. Achieving a low series resistance involves optimizing the metal contact to p-type InGaAs with a relatively high activated carrier concentration (> 10^{19} /cm^3)[26], increasing the thickness of the metal gridlines[11], and optimizing the grid pattern and dimension[29]. We emphasize that the reduced sensitivity to emitter temperature is achieved by the combination of high R_{OUT} and the multiterminal configuration enabled by the dual air-bridge tandem. A low temperature sensitivity is significant in the context of grid-scale electrical storage employing thermal batteries since it allows grid operators to widen the temperature differential within the storage medium, enabling actions such as discharging the thermal battery temperature to as low as 1000°C during periods of high demand, while incurring only marginal efficiency losses. This capability, in turn, has the potential to reduce the required amount of storage material.

To illustrate the impact of the extended temperature range, we calculate the cost per unit energy (CPE) of the graphite energy storage medium. The CPE is the cost per kg of graphite (US \$0.5/kg[30]) divided by the energy stored per mass, which is given by the integral of the graphite heat capacity and the TPV efficiency over the range of emitter temperatures encountered during the cooling/discharge phase. Figure 5(c) shows that the use of an air-bridge tandem lowers the CPE by approximately 50% compared to an analogous tunnel-junction tandem, from 6.91/kWh to \$3.96/kWh at a temperature swing of 600°C.

The TPV efficiency of the tunnel-junction tandem is described in Supporting Information 6. These CPE reductions should translate to other energy storage components of thermal batteries, including insulation, since the cells govern the denominator of the CPE. The calculation assumes a 600ºC graphite temperature swing and that the cells have the same electrical cell parameters (*i.e.*, shunt and series resistances, dark current densities). Although the tandem air-bridge process requires separate wafers to grow each sub-cell, the differential cost associated with this approach can almost entirely be mitigated using non-destructive epitaxial lift-off which allows for multiple reuses of the growth wafer[31–33]. Therefore, the potential to substantially lower the overall CPE, while maintaining comparable cost per power (CPP), suggests that air-bridge tandems can play a key role in the broad deployment of economical thermal batteries for long-duration grid-scale electrical storage.

Our study has successfully demonstrated air-bridge III-V tandem TPV cells fabricated through low-temperature cold welding of individual III-V ultrathin film air-bridge subcells, thereby eliminating the need for tunnel junctions. Incorporating two air bridges and a multiterminal configuration, the tandem cells achieve lossless optical transmission between the subcells. We achieved a R_{OUT} = 97.2%, accompanied by a higher P_{MPP} when operated in a multiterminal configuration compared to a two-terminal tandem operation. As a result, a single 0.74 eV bandgap InGaAs air-bridge cell shows 36.0% efficiency, while air-bridge homotandem cells achieve 37.8%, and 39.3% for the 0.90/0.74 eV heterotandem cells. With the enhancement of R_{s}, a dual air-bridge tandem cell is projected to achieve an efficiency exceeding the 45%. This innovative approach to the air-bridge tandem structure is anticipated to stimulate further cell optimization with a low temperature sensitivity, paving the way for the development of cost-effective, high-power density, and highly efficient TPV cells.

Methods

Image process using a scanning electron microscope. The SEM image was captured using a field emission SEM (Hitachi SU8000 In-Line). The sample was mounted on a holder at 45°. The holder was further tilted by an additional 45° to obtain a cross-sectional view of the air-bridge structure. A 10 kV accelerating voltage and 2.3μA emission current were utilized during the imaging process.

Spectral efficiency. The spectral efficiency is calculated using:

$$\mathrm{SE} = \frac{E_{\mathrm{g,top}} \int_{\mathrm{E_{g,top}}}^{\infty} \varepsilon_{\mathrm{eff,top}}(E) \cdot \Phi_{\mathrm{B}}(E, T_{\mathrm{h}}) \mathrm{d}E + E_{\mathrm{g,bot}} \int_{E_{\mathrm{g,bot}}}^{\infty} \varepsilon_{\mathrm{eff,bot}}(E) \cdot \Phi_{\mathrm{B}}(E, T_{\mathrm{h}}) \mathrm{d}E}{\int_{0}^{\infty} \varepsilon_{\mathrm{eff,T}}(E) \cdot E \cdot \Phi_{\mathrm{B}}(E, T_{\mathrm{h}}) \mathrm{d}E},$$

where $\varepsilon_{\mathrm{eff,T}}(E) = \frac{(1-R_{\mathrm{e}})A_{\mathrm{c,T}}}{1-R_{\mathrm{e}}(1-A_{\mathrm{c,T}})}$ is the effective emissivity of the cavity formed by the emitter and the tandem cell, R_{e} is spectral reflectance of the emitter, and $A_{\mathrm{c,top}}$ and $A_{\mathrm{c,bot}}$ are the absorptance for the top and bottom cells in the tandem structure, respectively.

External quantum efficiency. EQE measurements are conducted with monochromatic illumination, chopped at 200 Hz, and directed into a multimode SMA fiber connector to a bare fiber optic patch cable (M118L02, Thorlabs) set at a 15° angle to the TPV cells. The output signal is monitored and collected by a SR830 lock-in amplifier. Calibration of the illumination power is performed using a 818-UV/DB Si detector (Newport) from 400 nm to 900 nm, a 818-IG InGaAs detector (Newport) from 900 nm to 1,650 nm, and a FDG03 Ge detector (Thorlabs) from 1,650 nm to 1,800 nm.

Electrical characterization. The TPVs are mounted on a copper plate coupled with a closed-loop water chiller, maintaining the temperature at 20°C[3,6]. Using a three-axis translational stage, a SiC globar emitter (SLS203, Thorlabs Inc.) is centered over the sample and vertically translated to control the distance from emitter to cell. The emitter spectral emissivity (ε_e) is calibrated by referencing to a true blackbody source (IR-564, Infrared Systems Development Corp.). The black body shows $\varepsilon_e > 0.99$, whereas the ε_e of the SiC emitter was measured to be 0.96. The *J-V* curves are characterized using a Keithley 2401 Source Measure Unit in the 4-wire sensing mode.

TPV efficiency. The efficiency of a tandem TPV cell is the ratio of the power produced, P_{MPP}, to the heat absorbed, Q_{abs}, by the tandem cell, viz. $\eta_{\mathrm{TPV}} = \frac{P_{\mathrm{MPP}}}{Q_{\mathrm{abs}}}$. The efficiencies of the sub-cells are the power produced in each subcell, divided by the heat absorbed by the tandem cell. The heat absorbed Q_{abs} is the difference between the incident and reflected powers on the cell. The reflected power P_{ref} is determined using:

$$P_{\mathrm{ref}} = F_{\mathrm{v}} \int_0^{\infty} (1 - \varepsilon_{\mathrm{eff}}(E)) \cdot E \cdot \Phi_{\mathrm{B}}(E, T_{\mathrm{h}}) \; dE$$

This approach does not involve direct measurement of heat absorbed with a calorimeter, as has been done in prior publications.[8,11,12,34]. However, it has been demonstrated to agree with the calorimetry method of efficiency measurement[11,12]. In this study, we have taken efforts to mitigate the weaknesses of this technique, including (1) accounting for angular dependence on efficiency as demonstrated in Supporting Information 2, (2) cell temperature is controlled between 23°C and 32°C to reduce the possibility of *operando* changes in radiative characteristics, including bandgap narrowing, (3) ensuring that the radiative properties before and after testing are constant; (4) measured the spectral emittance of the heat source in operation. The calculated apparent view factors are 0.34 and 0.33 for the homo- and heterotandem devices, respectively.

Error propagation. Uncertainties in the reported experimental quantities are evaluated based on propagation of the following errors: variance using a t-distribution with a 95% confidence interval, instrument error and resolution error. All errors are assumed to be uncorrelated.

ASSOCIATED CONTENT

Supporting Information. Structure and fabrication, Optical properties of tandem TPVs, Complete experimental data for homotandem, Near term improvement to efficiency for homotandem cell, Complete experimental data for heterotandem, Tunnel-junction tandem TPV efficiency

ACKNOWLEDGEMENTS

The authors thank the Lurie Nanofabrication Facility at the University of Michigan. This research was sponsored by the Army Research Office (ARO) under Grant Number W911NF-18-1-0004 and the National Science Foundation (NSF) under Grant Number 2018572. The views and conclusions contained in this document are those of the authors and should not be interpreted as representing the official policies, either expressed or implied, of the ARO or the U.S. Government. The U.S. Government is authorized to reproduce and distribute reprints for Government purposes notwithstanding any copyright notation herein.

Conflict of Interest

The authors do not have any conflict of interest to disclose.

Date and materials availability statement

The data and materials that support the findings of this study are available from the corresponding authors upon reasonable request.

References

1. Bierman, D. M. *et al.* Enhanced photovoltaic energy conversion using thermally based spectral shaping. *Nat Energy* **1**, 16068 (2016).

2. Amy, C., Seyf, H. R., Steiner, M. A., Friedman, D. J. & Henry, A. Thermal energy grid storage using multi-junction photovoltaics. *Energy Environ Sci* **12**, 334–343 (2019).

3. Fan, D. *et al.* Near-perfect photon utilization in an air-bridge thermophotovoltaic cell. *Nature* **586**, 237–241 (2020).

4. Lee, B. *et al.* Air-Bridge Si Thermophotovoltaic Cell with High Photon Utilization. *ACS Energy Lett* **7**, 2388–2392 (2022).

5. Burger, T., Sempere, C., Roy-Layinde, B. & Lenert, A. Present Efficiencies and Future Opportunities in Thermophotovoltaics. *Joule* **4**, 1660–1680 (2020).

6. Roy-Layinde, B. *et al.* Sustaining efficiency at elevated power densities in InGaAs airbridge thermophotovoltaic cells. *Solar Energy Materials and Solar Cells* **236**, 111523 (2022).

7. Omair, Z. *et al.* Ultraefficient Thermophotovoltaic Power Conversion by Band-Edge Spectral Filtering. *Proc. Natl. Acad. Sci. U. S. A.* **116**, 15356 (2019).

8. Narayan, T. C. *et al.* Platform for Accurate Efficiency Quantification of > 35% Efficient Thermophotovoltaic Cells. in *2021 IEEE 48th Photovoltaic Specialists Conference (PVSC)* 1352–1354 (2021). doi:10.1109/PVSC43889.2021.9518588.

9. Arulanandam, M. K. *et al.* GaAs thermophotovoltaic patterned dielectric back contact devices with improved sub-bandgap reflectance. *Solar Energy Materials and Solar Cells* **238**, 111545 (2022).

10. Lim, J., Roy-Layinde, B., Liu, B., Lenert, A. & Forrest, S. R. Enhanced Photon Utilization in Single Cavity Mode Air-Bridge Thermophotovoltaic Cells. *ACS Energy Lett* **8**, 2935–2939 (2023).

11. Tervo, E. J. *et al.* Efficient and scalable GaInAs thermophotovoltaic devices. *Joule* **6**, 2566–2584 (2022).

12. LaPotin, A. *et al.* Thermophotovoltaic efficiency of 40%. *Nature* **604**, 287–291 (2022).

13. Schulte, K. L. *et al.* Inverted metamorphic AlGaInAs/GaInAs tandem thermophotovoltaic cell designed for thermal energy grid storage application. *J Appl Phys* **128**, 143103 (2020).

14. Feldmann, F. *et al.* Carrier-selective contacts for Si solar cells. *Appl Phys Lett* **104**, 181105 (2014).

15. D'Rozario, J. R., Polly, S. J., Nelson, G. T., Wilt, D. & Hubbard, S. M. Modeling free-carrier absorption in ultrathin III-V solar cells with light management. *Opt Express* **30**, 7096–7109 (2022).

16. Burger, T. *et al.* Semitransparent thermophotovoltaics for efficient utilization of moderate temperature thermal radiation. *Proceedings of the National Academy of Sciences* **119**, e2215977119 (2022).

17. Hagar, B. G., Sayed, I., Colter, P. C., El-Masry, N. A. & Bedair, S. M. A new approach for Multi junction solar cells from off the shelf individual cells: GaAs/Si. in *2019 IEEE 46th Photovoltaic Specialists Conference (PVSC)* 994–997 (2019). doi:10.1109/PVSC40753.2019.8980696.

18. Lim, J. & Forrest, S. R. Limits to the Energy-Conversion Efficiency of Air-Bridge Thermophotovoltaics. *Phys Rev Appl* **19**, 34099 (2023).

19. Dawidowski, W. *et al.* Tunnel junction limited performance of InGaAsN/GaAs tandem solar cell. *Solar Energy* **214**, 632–641 (2021).

20. Schulte, K. L. *et al.* Inverted metamorphic AlGaInAs/GaInAs tandem thermophotovoltaic cell designed for thermal energy grid storage application. *J Appl Phys* **128**, 143103 (2020).

21. Lim, J., Fan, D., Lee, B. & Forrest, S. R. Understanding and Control of Compressively Buckled Semiconductor Thin Films. *Phys Rev Appl* **16**, 64010 (2021).

22. Johnson, E. J. & Fan, H. Y. Impurity and Exciton Effects on the Infrared Absorption Edges of III-V Compounds. *Physical Review* **139**, A1991–A2001 (1965).

23. Schnabel, M. *et al.* Equivalent Performance in Three-Terminal and Four-Terminal Tandem Solar Cells. *IEEE J Photovolt* **8**, 1584–1589 (2018).

24. Warren, E. L. *et al.* Maximizing tandem solar cell power extraction using a three-terminal design. *Sustainable Energy Fuels* **2**, 1141–1147 (2018).

25. Warren, E. L. *et al.* A Taxonomy for Three-Terminal Tandem Solar Cells. *ACS Energy Lett* **5**, 1233–1242 (2020).

26. Lin, J. C., Yu, S. Y. & Mohney, S. E. Characterization of low-resistance ohmic contacts to n- and p-type InGaAs. *J Appl Phys* **114**, 044504 (2013).

27. Crook, A. M. *et al.* Low resistance, nonalloyed Ohmic contacts to InGaAs. *Appl Phys Lett* **91**, 192114 (2007).

28. Nishioka, K. *et al.* Evaluation of InGaP/InGaAs/Ge triple-junction solar cell and optimization of solar cell's structure focusing on series resistance for high-efficiency concentrator photovoltaic systems. *Solar Energy Materials and Solar Cells* **90**, 1308–1321 (2006).

29. Liu Wen *et al.* Optimization of grid design for solar cells. *Journal of Semiconductors* **31**, 014006 (2010).

30. Kelsall, C. C., Buznitsky, K. & Henry, A. *Technoeconomic Analysis of Thermal Energy Grid Storage Using Graphite and Tin*.

31. Lee, B., Fan, D. & Forrest, S. R. A high throughput, linear molecular beam epitaxy system for reduced cost manufacturing of GaAs photovoltaic cells: will GaAs ever be inexpensive enough? *Sustain Energy Fuels* **4**, 2035–2042 (2020).

32. Lee, K., Zimmerman, J. D., Hughes, T. W. & Forrest, S. R. Non-Destructive Wafer Recycling for Low-Cost Thin-Film Flexible Optoelectronics. *Adv Funct Mater* **24**, 4284–4291 (2014).

33. Lee, K., Shiu, K. T., Zimmerman, J. D., Renshaw, C. K. & Forrest, S. R. Multiple growths of epitaxial lift-off solar cells from a single InP substrate. *Appl Phys Lett* **97**, 10–12 (2010).

34. Swanson, R. M. Recent developments in thermophotovoltaic conversion. *1980 International Electron Devices Meeting* 186–189 (1980) doi:10.1109/IEDM.1980.189789.

Supporting Information

Integrated air-bridge tandem thermophotovoltaics with high efficiency over a broad heat source temperature range

Bosun Roy-Layinde[1,4], Jihun Lim[2,4], Andrej Lenert[2], and Stephen R. Forrest[2,3*]

[1]Department of Chemical Engineering, University of Michigan, Ann Arbor, MI 48109

[2]Department of Electrical Engineering and Computer Science, University of Michigan, Ann Arbor, MI 48109

[3]Department of Physics and Materials Science and Engineering, University of Michigan, Ann Arbor, MI 48109

[4]These authors contributed equally: Bosun Roy-Layinde, Jihun Lim.

[*]Corresponding authors: Stephen R. Forrest (stevefor@umich.edu), Andrej Lenert (alenert@umich.edu)

S1. Structure and fabrication

S1.1 Epitaxial layer structure

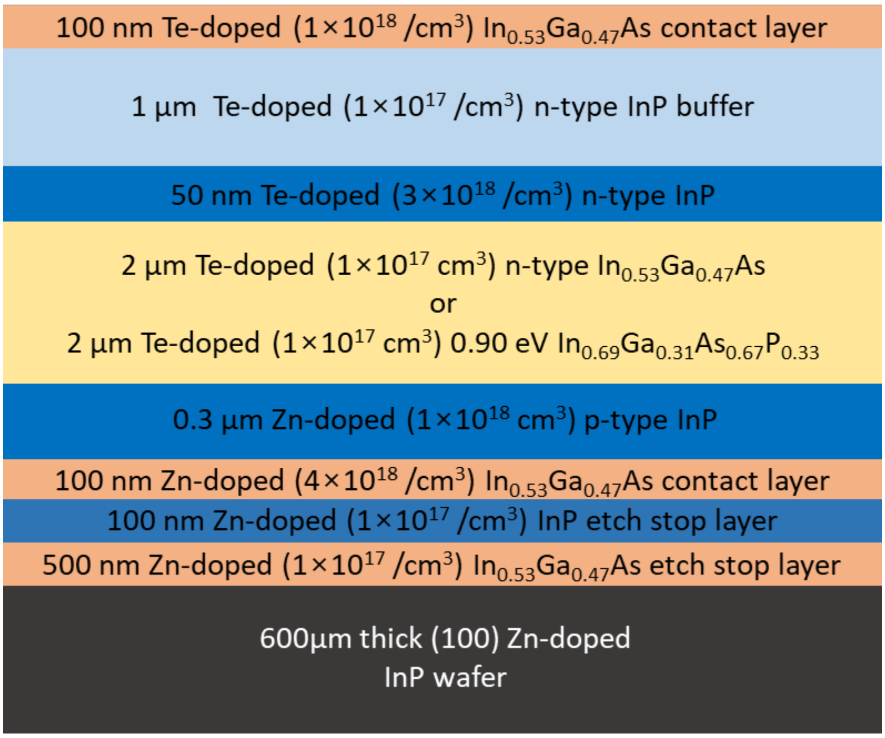

Figure S1.1. Air-bridge tandem thermophotovoltaic structure. The lattice-matched III-V epitaxial layers are grown by metalorganic chemical vapor deposition on a 600µm thick (100) Zn-doped InP substrate (Microlink Devices Inc., Niles, IL, USA).

S1.2 Key fabrication steps

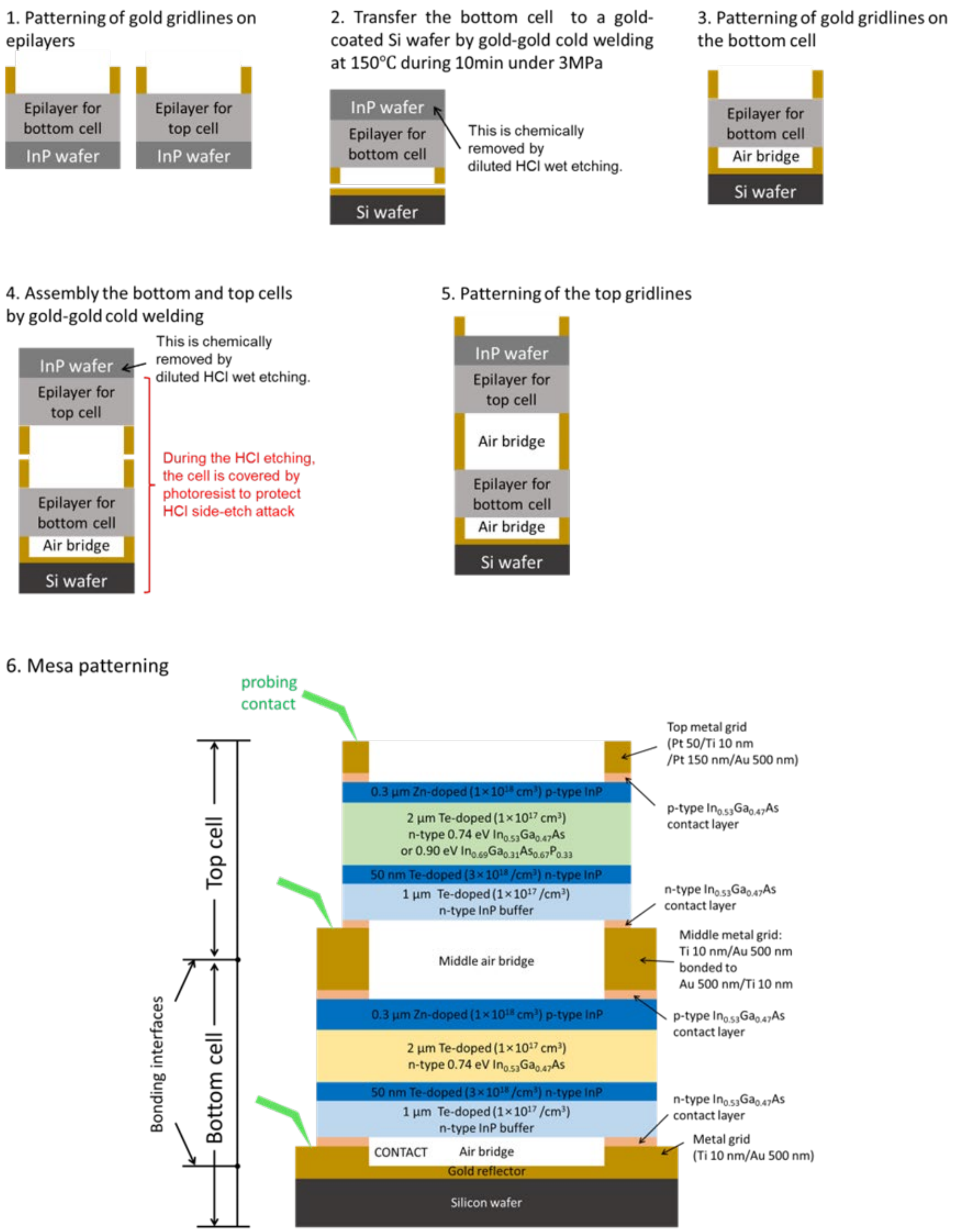

Figure S1.2. Fabrication process flow, including patterning and metal liftoff processes.

S2. Optical properties of tandem TPVs

S2.1. Out-of-band simulation for six different TPV cells

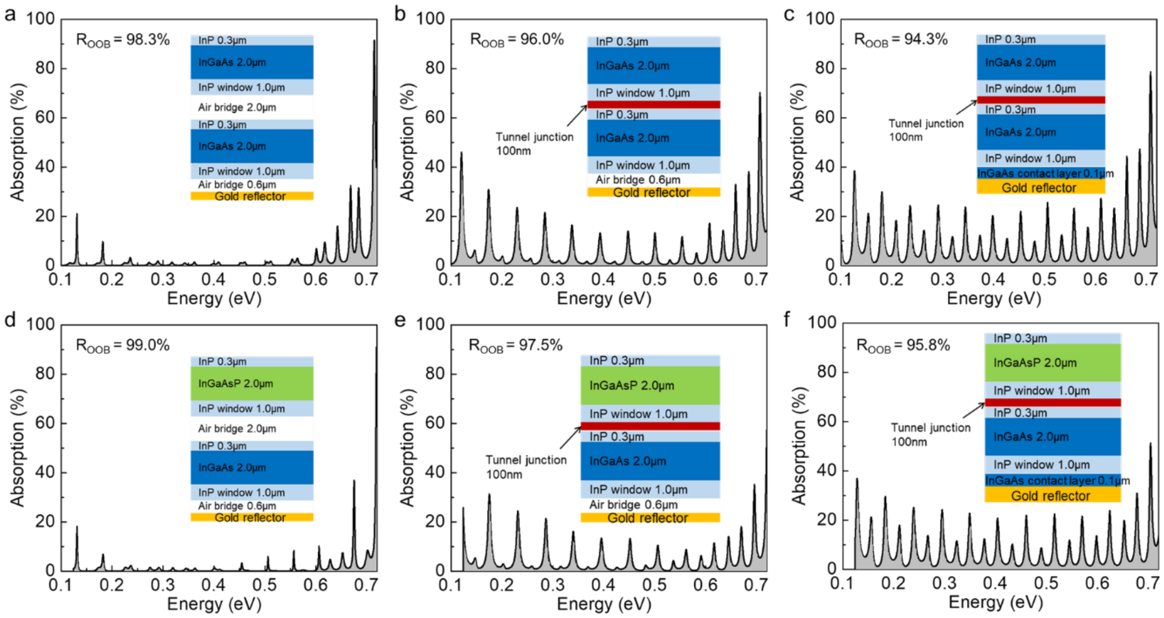

Figure S2.1. Simulation of out-of-band absorption. Out-of-band optical properties for six different TPV tandem structures determined using transfer-matrix method simulations. The 100-nm-thick tunnel junction assumes the InGaAs layers with $10^{20}/cm^3$ n-type carrier concentrations, which causes the intraband transitions of free carriers based on Drude theory described in our previous work[2,3].

Lattice-matched InGaAs and InGaAsP epitaxial layers are grown on InP wafers by metal-organic chemical vapor deposition. Full layer structures are described in Supplementary Information 1. The air-bridge InGaAs bottom cell is prepared as in previous work[3]. Next, Au grids are patterned on the InGaAsP wafer using e-beam evaporation and metallization patterned via liftoff. The Au grids are optically aligned and bonded with the top Au grids on the InGaAs cell using a flip-chip bonder (Fineplacer lambda, Finetech Inc., USA). The bonding is conducted for 10 min at a pressure and temperature of 200 N and 150°C, respectively. The top InP wafer is chemically removed in deionized water:HCl = 1:1. The 1×1 cm^2 square TPV mesa is subsequently patterned by alternatively wet-etching InGaAsP using H_2O_2:H_2SO_4:H_2O, InGaAs in H_2O_2:H_2PO_4:H_2O, and InP in HCl:H_2O. Finally, the top metal grids (Ti/Au 10nm/500nm) are patterned by e-beam evaporation and patterned using liftoff.

Table S2.1. Out-of-band reflectance vs emitter temperatures for various tandems.

Temp. (°C)	AB 0.74 eV InGaAs	AB 0.92eV InGaAsP	AB Homotandem	AuBSR Homotandem	AB Heterotandem	AuBSR Heterotandem
927	98.89	99.26	98.60	92.74	99.08	93.12
1027	98.75	99.21	98.42	92.67	99.00	93.14
1127	98.61	99.16	98.23	92.59	98.92	93.14
1227	98.49	99.12	98.04	92.50	98.84	93.13
1327	98.37	99.08	97.87	92.40	98.77	93.12
1427	98.26	99.05	97.70	92.30	98.70	93.09
1527	98.16	99.03	97.55	92.21	98.63	93.06

S2.2. Modeled spectral efficiency

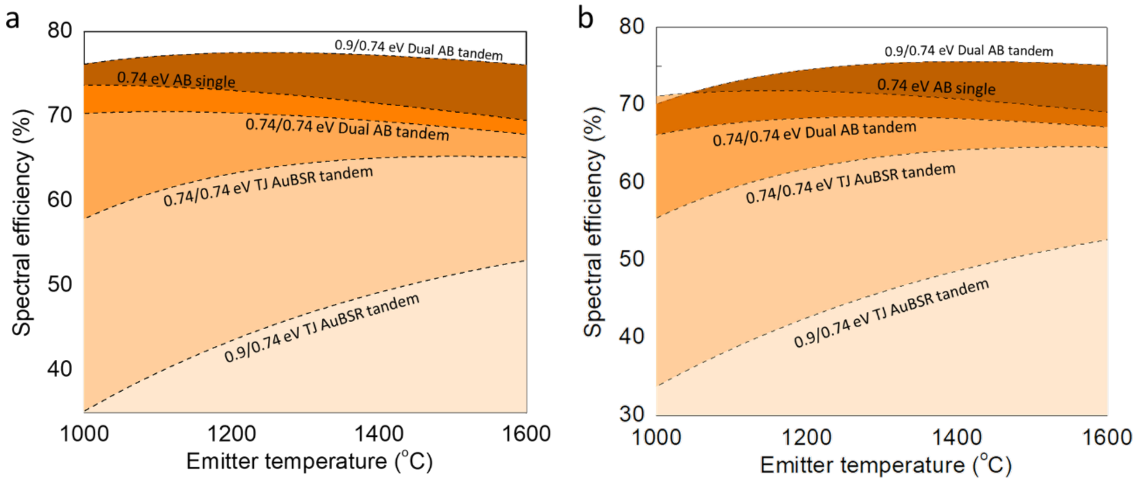

Figure S2.2. Spectral efficiency (a) without FCA and (b) with FCA model.

S2.3. Comparison of optical model to experiments:

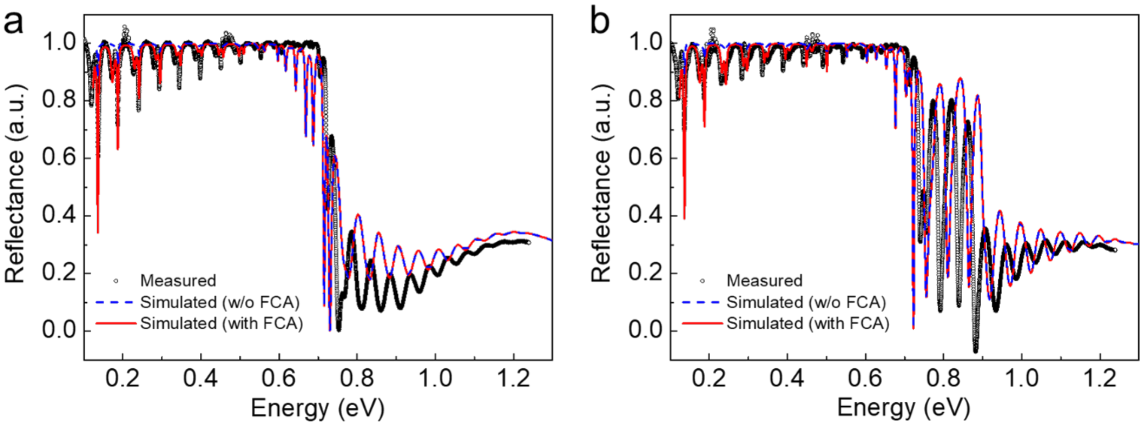

Figure S2.3. Optical measurements and simulations for (a) 0.74/0.74 eV and (b) 0.90/0.74 eV tandem cells, respectively.

Reflectance measurements on the TPV samples were performed using a Cary 670-IR spectrometer with a Cary 620 IR microscope (Agilent Technologies, CA), equipped with globar near- and mid-IR sources, a 15× objective, and a liquid nitrogen-cooled HgCdTe (MCT) detector. All data are collected at 1 cm^{-1} spectral resolution. Experimental out-of-band reflectance (R_{OUT}), which is the average reflectance when weighted to an emitter spectrum, for the tandem cells is calculated from the FTIR measurements as:

$$R_{\mathrm{OUT}} = \frac{\int_0^{E_\mathrm{g}} R(E) \cdot E \cdot \Phi_\mathrm{B}(E,T_\mathrm{h})\, dE}{\int_0^{E_\mathrm{g}} E \cdot \Phi_\mathrm{B}(E,T_\mathrm{h})\, dE}$$

where $\Phi_\mathrm{B}(E,T_\mathrm{h})$ is the spectral photon flux of the heat source, $R(E)$ the measured spectral reflectance of the tandem cell, E is the photon energy, T_h is the emitter temperature and, E_g is the cell bandgap.

S2.4. Effects of hemispherical integration on performance

Table S2.4. Simulated angular dependence of out-of-band reflectance and efficiencies for the (a) homotandem, and (b) heterotandem air-bridge cells at their optimal emitter temperatures.

(a) Homotandem

Integration angle (°)	Out-of-band reflectance (%)	Peak efficiency (%)
15 (single angle)	96.6	38.2
0 to 60	96.5	38.0
0 to 90	96.4	37.8

(b) Heterotandem

Integration angle (°)	Out-of-band reflectance (%)	Peak efficiency (%)
15 (single angle)	97.6	40.3
0 to 60	97.7	40.6
0 to 90	97.6	40.3

S3. Complete experimental data for homotandem

S3.1. Current-voltage (*J-V*) characteristics:

Table S3.1. Variation in measured open-circuit voltage (V_{oc}), short-circuit current (J_{sc}), fill factor (FF), and power density (P_{mpp}) versus emitter temperature (T_h) for the (a) top cell, (b) bottom cell, and (c) two-terminal operation in the homotandem configuration.

(a) Top cell

T_h (°C)	J_{sc} (mA/cm^2)	V_{oc} (mV)	FF (%)	P_{mpp} (mW/cm^2)
959	275.75	518.69	76.605	109.57
1039	453.53	529.99	75.187	180.73
1116	698.18	539.63	73.228	275.89
1191	1013.4	548.01	71.333	396.13
1265	1421	553.65	69.654	548.01
1341	1953.5	559.06	67.442	736.57

(b) Bottom cell

T_h (°C)	J_{sc} (mA/cm^2)	V_{oc} (mV)	FF (%)	P_{mpp} (mW/cm^2)
959	91.583	473.72	70.719	30.681
1039	146.44	484.87	68.028	48.303
1116	220.55	492.12	64.23	69.713
1191	312.26	499.99	60.151	93.911
1265	427.76	505.24	56.016	121.06
1341	569.98	510.26	52.826	153.64

(c) Two-terminal homotandem

T_h (°C)	J_{sc} (mA/cm^2)	V_{oc} (mV)	FF (%)	P_{mpp} (mW/cm^2)
959	90.124	992.21	79.586	71.167
1039	146.77	1015.2	77.603	115.64
1116	219.82	1032	74.624	169.29

1191	315.16	1047.5	70.381	232.34
1265	433.06	1060	66.072	303.29
1341	585.44	1070	61.536	385.47

S3.2. Performance metrics for the homotandem cell

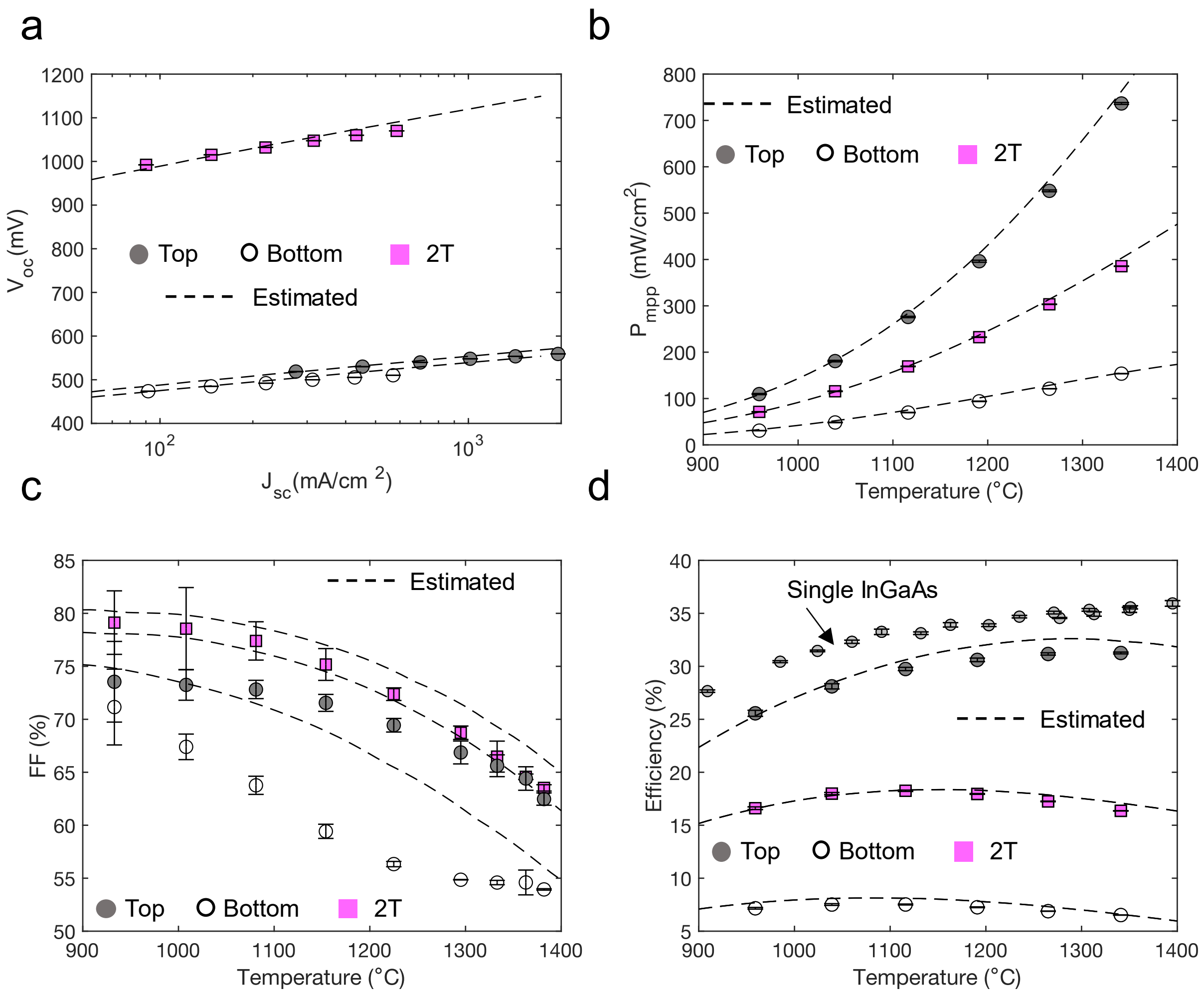

Figure S3.2. 0.74/0.74 eV InGaAs homotandem cell characterization. a. Short-circuit current density (J_{sc}) versus emitter temperature. b. Max-power point (P_{mpp}) versus emitter temperature. c. Fill factor (FF) versus emitter temperature. d. TPV efficiency versus emitter temperature.

Cell parameters are determined by fitting the following expression to the measured *J-V* characteristics:

$$J = J_1\left[\exp\left(\frac{q(V-R_sJ)}{k_bT_c}\right)-1\right]+J_2\left[\exp\left(\frac{q(V-R_sJ)}{2k_bT_c}\right)-1\right]+\frac{V-R_sJ}{R_{sh}}-J_{ph},$$

where J_1 and J_2 are the saturation current densities for diffusion and recombination-limited current sources, respectively. J_{ph} is the photocurrent density, T_c is the cell temperature, and k_b is the Boltzmann constant. R_s and R_{sh} are the series and shunt resistances, respectively. J_{ph} is estimated by measuring the *J-V* under the heat emission using a SiC globar emitter. The R_s for the top cell is 45mΩ-cm^2 while the R_s of the bottom cell is 130mΩ-cm^2.

S4. Near-term improvement to efficiency for homotandem cell

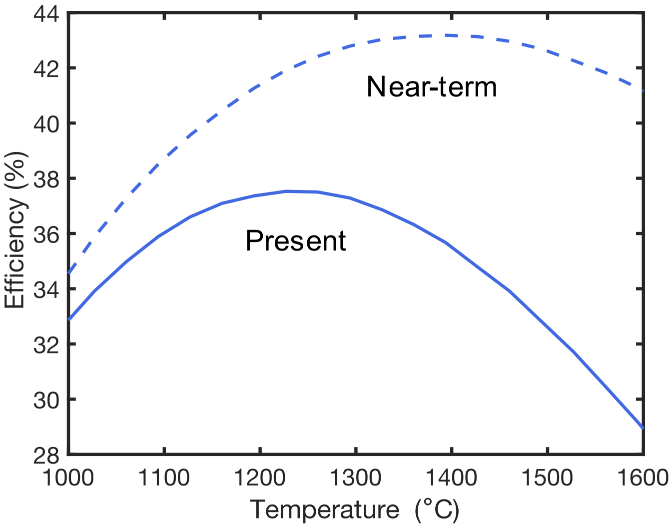

Figure S4. Present day efficiency for the multi-terminal homotandem cell vs emitter temperature, and that expected with reduction in cell series resistance to 15mΩ-cm^2.

S5. Complete experimental data for heterotandem

S5.1. Current-voltage (*J-V*) characteristics

Table S5.1. Variation in measured open-circuit voltage (V_{OC}), short-circuit current (J_{SC}), fill factor (*FF*), and power density (P_{mpp}) versus emitter temperature (T_h) for the (a) top cell, (b) bottom cell, and (c) two-terminal operation in the heterotandem configuration.

(a) Top cell

T_h (°C)	J_{sc} (mA/cm^2)	V_{oc} (mV)	FF (%)	P_{mpp} (mW/cm^2)
933	73.453	589.97	73.542	31.869
1008	130.78	601.3	73.247	57.599
1081	212.4	621.49	72.814	96.119
1154	324.98	632.33	71.55	147.03
1225	477.03	641.33	69.438	212.44
1295	678.36	649.01	66.868	294.4
1333	810.04	651.2	65.615	346.12
1363	927.64	655.23	64.409	391.49
1382	1004.7	644.15	62.47	404.3
1414	1146.1	659.01	62.478	471.87
1434	1256.6	646.36	60.48	491.23

(b) Bottom cell

T_h (°C)	J_{sc} (mA/cm^2)	V_{oc} (mV)	FF (%)	P_{mpp} (mW/cm^2)
933	147.06	468.73	71.154	49.046
1008	241.13	477.78	67.398	77.648
1081	362.43	491.51	63.767	113.59
1154	516.61	499.96	59.424	153.48

1225	704.83	506.23	56.332	201
1295	911.44	510	54.856	254.99
1333	1026.4	513.5	54.589	287.72
1363	1126	515.35	54.598	316.83
1382	1221.1	505.82	53.941	333.18
1414	1281	517.42	54.765	363
1434	1402.9	506.44	54.468	386.99

(c) Two-terminal heterotandem

T_h (°C)	J_{sc} (mA/cm^2)	V_{oc} (mV)	FF (%)	P_{mpp} (mW/cm^2)
933	74.468	1062.5	79.126	62.607
1008	130.61	1075.7	78.553	110.37
1081	212.92	1113.9	77.397	183.56
1154	328.41	1135.1	75.173	280.22
1225	482.01	1148.6	72.372	400.68
1295	684.17	1160.1	68.73	545.5
1333	816.59	1164.9	66.477	632.36
1363	929.99	1170.4	64.573	702.83
1382	1009.6	1150.4	63.525	737.8
1414	1157.5	1175.7	60.998	830.09
1434	1256.4	1151	59.592	861.8
1471	1448.9	1150.8	59.419	990.76

S5.2. Performance metrics for the heterotandem cell

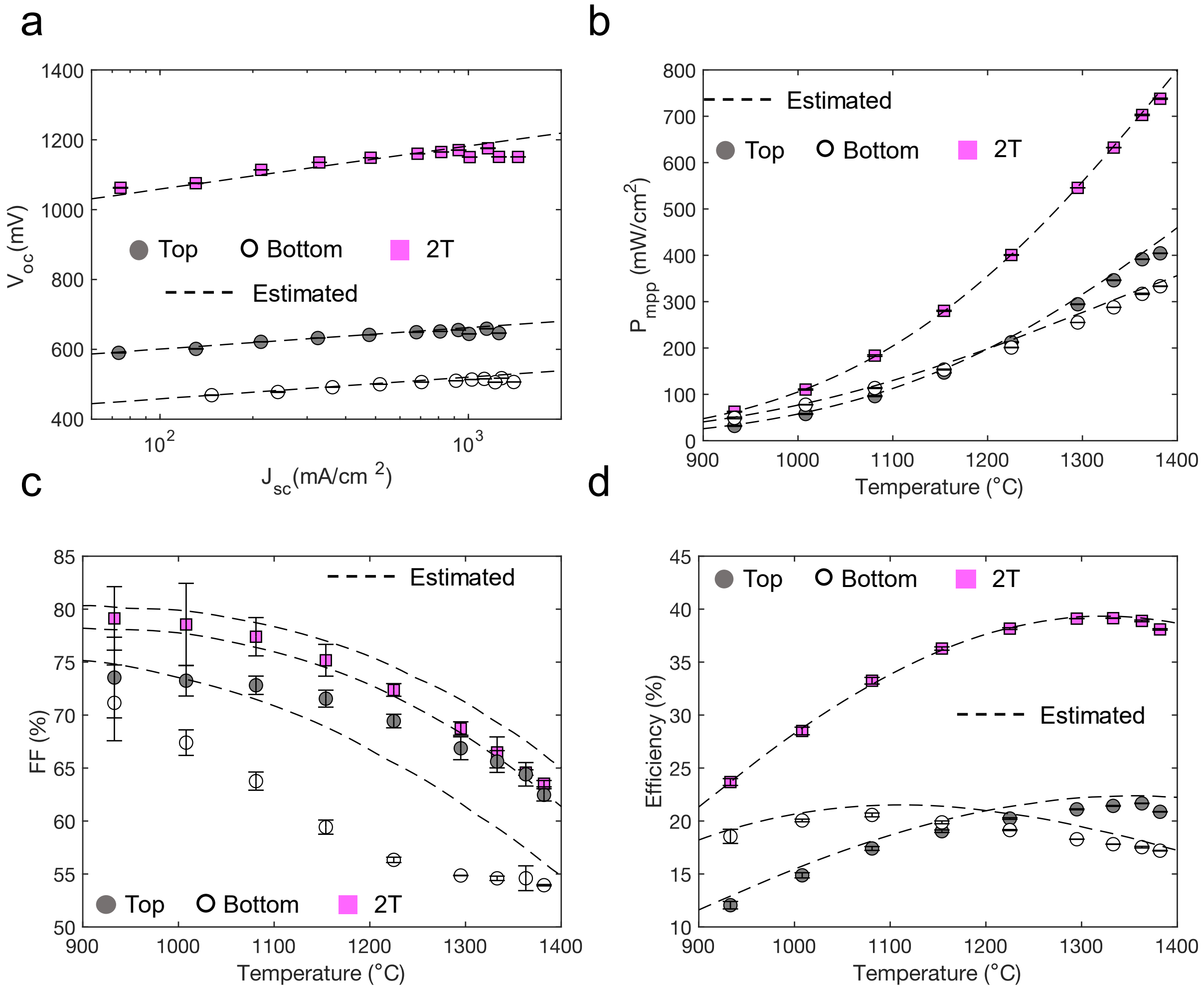

Figure S5.2. 0.90/0.74 eV InGaAsP/InGaAs heterotandem cell characterization. a. Short-circuit current density (J_{sc}) versus emitter temperature. b. Maximum power point (P_{mpp}) versus emitter temperature. c. Fill factor (FF) versus emitter temperature. d. TPV efficiency versus emitter temperature.

S6. TPV efficiency of a tunnel-junction tandem cell

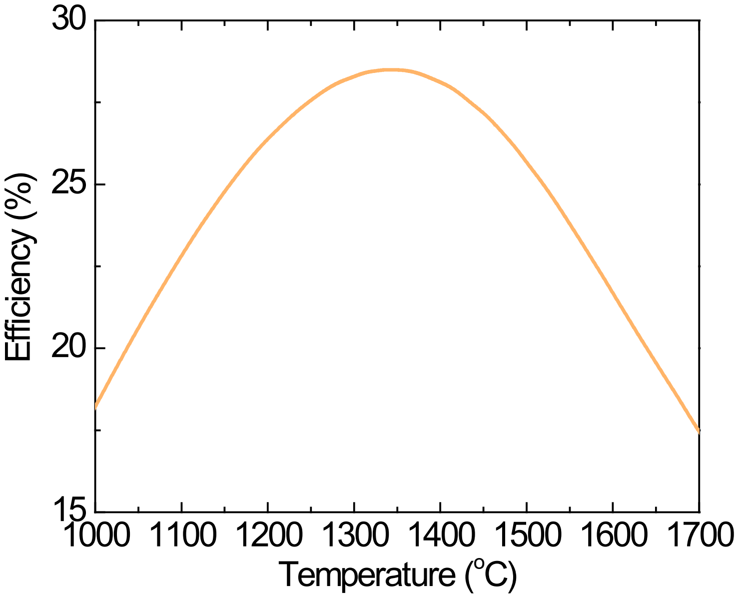

Figure S6. Simulated TPV efficiency of a tunnel-junction InGaAsP/InGaAs heterotandem cell. The calculation assumes the tunnel-junction tandem structure depicted in Figure S2.1(c). These same data are utilized to calculate the cost per unit energy in Figure 5(c).

References

1 Lim, J., Roy-Layinde, B., Liu, B., Lenert, A. & Forrest, S. R. Enhanced Photon Utilization in Single Cavity Mode Air-Bridge Thermophotovoltaic Cells. *ACS Energy Letters* **8**, 2935-2939 (2023).

2 Lim, J. & Forrest, S. R. Limits to the Energy-Conversion Efficiency of Air-Bridge Thermophotovoltaics. *Physical Review Applied* **19**, 034099 (2023).

3 Baker-Finch, S., McIntosh, K., Yan, D., Fong, K. & Kho, T. Near-infrared free carrier absorption in heavily doped silicon. *Journal of Applied Physics* **116** (2014).